



Die Grenzen der
Chemie neu ausloten?
It takes
#HumanChemistry

Wir suchen kreative Chemikerinnen und Chemiker,
die mit uns gemeinsam neue Wege gehen wollen –
mit Fachwissen, Unternehmertum und Kreativität für
innovative Lösungen. Informieren Sie sich unter:

[evonik.de/karriere](https://www.evonik.de/karriere)

Dual Ultrasound and Photoacoustic Tracking of Magnetically Driven Micromotors: From In Vitro to In Vivo

Azaam Aziz, Joost Holthof, Sandra Meyer, Oliver G. Schmidt, and Mariana Medina-Sánchez*

The fast evolution of medical micro- and nanorobots in the endeavor to perform non-invasive medical operations in living organisms has boosted the use of diverse medical imaging techniques in the last years. Among those techniques, photoacoustic imaging (PAI), considered a functional technique, has shown to be promising for the visualization of micromotors in deep tissue with high spatiotemporal resolution as it possesses the molecular specificity of optical methods and the penetration depth of ultrasound. However, the precise maneuvering and function's control of medical micromotors, in particular in living organisms, require both anatomical and functional imaging feedback. Therefore, herein, the use of high-frequency ultrasound and PAI is reported to obtain anatomical and molecular information, respectively, of magnetically-driven micromotors in vitro and under ex vivo tissues. Furthermore, the steerability of the micromotors is demonstrated by the action of an external magnetic field into the uterus and bladder of living mice in real-time, being able to discriminate the micromotors' signal from one of the endogenous chromophores by multispectral analysis. Finally, the successful loading and release of a model cargo by the micromotors toward non-invasive in vivo medical interventions is demonstrated.

1. Introduction

Micro- and nanorobots (MNRs) offer the potential to operate inside the living body for various healthcare applications,^[1–3] as they possess the capacity of reaching hard-to-access locations, non-invasively. Applications such as targeted drug delivery,^[4–7] biopsy,^[8] blood clot removal,^[9] or cell transport^[10] have been addressed, for example, by functionalizing the MNRs with biomolecules (e.g., bioreceptors or contrast agents) or by employing smart materials and designs to effectively transport and release a cargo (e.g., cells or drugs).^[1,11–17] Some of these micromotors have already been examined in ex vivo and in vivo environments. However, there are still significant limitations when steering single or swarms of MNRs in living organisms,^[2,18] in particular when the intended application and micromotor type require high spatiotemporal resolution imaging with precise anatomical positioning.


Each imaging technique has its limitations and therefore, researchers are rendering particular efforts to develop or implement imaging systems that could enable precise localization and control within biological tissues. So far, various imaging modalities have been evaluated for the monitoring of MNRs, including ultrasound (US), magnetic resonance imaging (MRI), positron emission tomography-computed tomography (PET-CT), and single-photon emission computed tomography (SPECT), in phantom, ex vivo or in vivo scenarios.^[19–24] MRI, for instance, has better imaging contrast for soft tissues than other conventional techniques, but its spatiotemporal resolution is insufficient to visualize small MNRs in real-time (below 100 μm). US is suitable for high imaging depth but lacks molecular specificity and image contrast. Besides, CT provides deep tissue penetration but has low temporal resolution and long-term exposures might harm the living organism. PET and SPECT provide high sensitivity and molecular information, but the radiation dose remains the foremost concern when an extended use is required to monitor MNRs. Additionally, optical methods including fluorescence,^[25] reflection-based IR imaging,^[26] or optical coherence tomography (OCT),^[27] have been used to track MNRs below scattering tissues with excellent spatiotemporal resolution but have been limited to sub-skin level or superficial medical applications (typically $\approx 1\text{--}2$ mm in thick biological

A. Aziz, O. G. Schmidt, M. Medina-Sánchez
Institute for Integrative Nanosciences
Leibniz IFW Dresden
Helmholtzstrasse 20, 01069 Dresden, Germany
E-mail: m.medina.sanchez@ifw-dresden.de

J. Holthof, S. Meyer
FUJIFILM VisualSonics Inc.
Amsterdam 1114 AB, The Netherlands

O. G. Schmidt
Center for Materials, Architectures and Integration of Nanomembranes (MAIN)
TU Chemnitz
Reichenhainer Strasse 10, 09107 Chemnitz, Germany

O. G. Schmidt
School of Science
TU Dresden
01062 Dresden, Germany

 The ORCID identification number(s) for the author(s) of this article can be found under <https://doi.org/10.1002/adhm.202101077>

© 2021 The Authors. Advanced Healthcare Materials published by Wiley-VCH GmbH. This is an open access article under the terms of the Creative Commons Attribution-NonCommercial License, which permits use, distribution and reproduction in any medium, provided the original work is properly cited and is not used for commercial purposes.

DOI: 10.1002/adhm.202101077

tissues).^[28,29] Unfortunately, in optical methods, spatial resolution degrades significantly with depth due to pronounced light scattering.

To preserve the spatial resolution and molecular specificity of optical techniques while enhancing the temporal resolution and penetration depth, scientists have developed a hybrid optical-ultrasound imaging technique, also called photoacoustic imaging (PAI).^[29–33] PAI is based on the photoacoustic effect first observed by Alexander Graham Bell in 1880,^[34] which in those days described the generation of sound waves by sunlight. Nowadays, PAI is based on short IR laser pulses which are used to excite tissues, inducing thermoelastic expansion/contraction that produces ultrasonic waves.^[35] Such ultrasonic waves travel through the tissue until being captured by ultrasensitive ultrasound detectors.^[29,30] The use of PAI for the visualization of moving medical micromotors was first suggested by our group in 2017.^[2] We visualized in real-time single magnetically driven conical micromotors (up to 100 μm long) in 3D, underneath ≈ 1 cm phantom and ex vivo chicken tissue samples, highlighting the limits of the technique and showing the advantages of using nanomaterials as labels with unique absorption spectrum to improve micromotors' image contrast and molecular specificity.^[36–38] In later studies, PAI was employed for guiding capsules containing catalytic micromotors in mice intestines as well as to track swarms of magnetic spiral-like micromotors to treat induced subcutaneous bacterial infection, also in mice.^[24,39] Both PAI studies showed the application of micromotors in vivo but there was no clear observation of them in real-time with a well-defined anatomical localization. Thus, complementary particulars such as morphology, functionality, and molecular composition are required to enhance the position accuracy of employed MNRs in deep tissue. In this study, we investigate the use of high-frequency ultrasound (HFUS) and PAI to monitor swimming micromotors' motion and function. In particular, we monitor single and a swarm of magnetically driven micromotors in different scenarios: phantoms, ex vivo, and in vivo (in mouse bladder and uterus). Real-time monitoring of bladder catheterization and the localization of the uterus to monitor micromotors during administration was also demonstrated. Moreover, multispectral imaging was employed to extract the specific absorption spectrum from each of the present entities (MNRs and biological tissues), being of crucial importance when operating in biological environments which contain a variety of chromophores or absorbing molecules that hinder the MNRs signal. We finally demonstrated the successful cargo-release of a model drug, doxorubicin (DOX), by the above-mentioned micromotors, while navigating onto a surface due to an applied rotating magnetic field. However, the suggested methods and settings can be easily extended to any other type of medical microrobot as long as their size (single or a swarm) is in the range of the spatial resolution of the employed technique and that it is made of an IR absorbing material, like thin metallic films or nanomaterials. With that, we prove the advantages of this technique to supervise and monitor both the position and function of medical microrobots in different scenarios, from in vitro, ex vivo to living mice.

2. Results and Discussion

2.1. Static Imaging of Single Micromotors

A multimodal HFUS and photoacoustic (PA) system equipped with a linear array ultrasound transducer and fiber optic bundles on either side of the transducer for illumination (680–970 nm) was used for the static imaging of single micromotors (Figure 1a and Table S1, Supporting Information). SiO_2 particles with a diameter of 100 μm were drop-casted onto a substrate, followed by the evaporation of subsequent thin metal layers (Ti = 10 nm, Fe = 50 nm, and Ti = 10 nm) (refer to the Experimental Section and Figure S1, Supporting Information). The analysis of particle size distribution was also performed for SiO_2 particles ($n = 260$), obtaining a mean diameter of 93.30 μm (standard deviation (SD) ± 7.7 μm) (Figure S2, Supporting Information). The particles were half-coated with metal layers by electron-beam deposition, resulting in what we call magnetically-driven micromotors (Figure 1bi). Figure 1bii shows the optical tracking of single/swarm of micromotors when actuated using an external permanent magnetic field (Figure S3, Supporting Information). The same micromotors can be actuated with rotating magnetic fields as was previously demonstrated by our group.^[26] Exemplary videos of single micromotors actuated by both magnetic field gradients and rotating magnetic fields are shown in Videos S1 and S2 respectively (Supporting Information). Figure 1biii shows a pseudo-colored scanning electron microscopy (SEM) image of the half-coated particle, highlighting the metal layer surface. Additionally, we loaded a model drug, DOX, onto the micromotors surface for further in vivo drug-release monitoring via PAI (Figure 1biv). Initially, we imaged static micromotors to evaluate the ability to locate a single of them by HFUS and PA system. The noted number of micromotors (3 in total) were transferred on an agarose surface after solidification as shown in the schematic and bright-field (BF) images (Figure 1ci,ii). Then, HFUS and PA signal amplitudes of the micromotors were recorded, resulting in a good agreement with the captured BF images (Figure 1ciii,iv). Since two of the micromotors were close to each other, their HFUS and PA response was higher than for individual micromotors, being possible to estimate the presence of multiple micromotors by their PA signal intensity. However, it was not possible to resolve individual micromotors when they were close to each other, due to the imaging system resolution. The absorbing metal layers provided a broad PA signal in the near infrared (NIR) region (with an excitation wavelength of 800 nm), where the fluence was set below the maximum permissible exposure (MPE) limit (20 mJ cm^{-2}) followed by the safe exposure guidelines.^[40]

To confirm the biocompatibility of the employed micromotors and materials, 3-(4,5-dimethylthiazol-2-yl)-5-(3-carboxymethoxyphenyl)-2-(4-sulfophenyl)-2H-tetrazolium (MTS) assay was performed using mesenchymal stem cells (MSCs) from bone marrow. The cell viability study of MSCs was conducted after being co-cultured with bare SiO_2 and metal-coated particles (micromotors), at 37 $^\circ\text{C}$ for 48 h, resulting in an increase of cell number on all the evaluated materials, showing non-evident toxicity (Figure 1d). The control group proceeded without any particles.

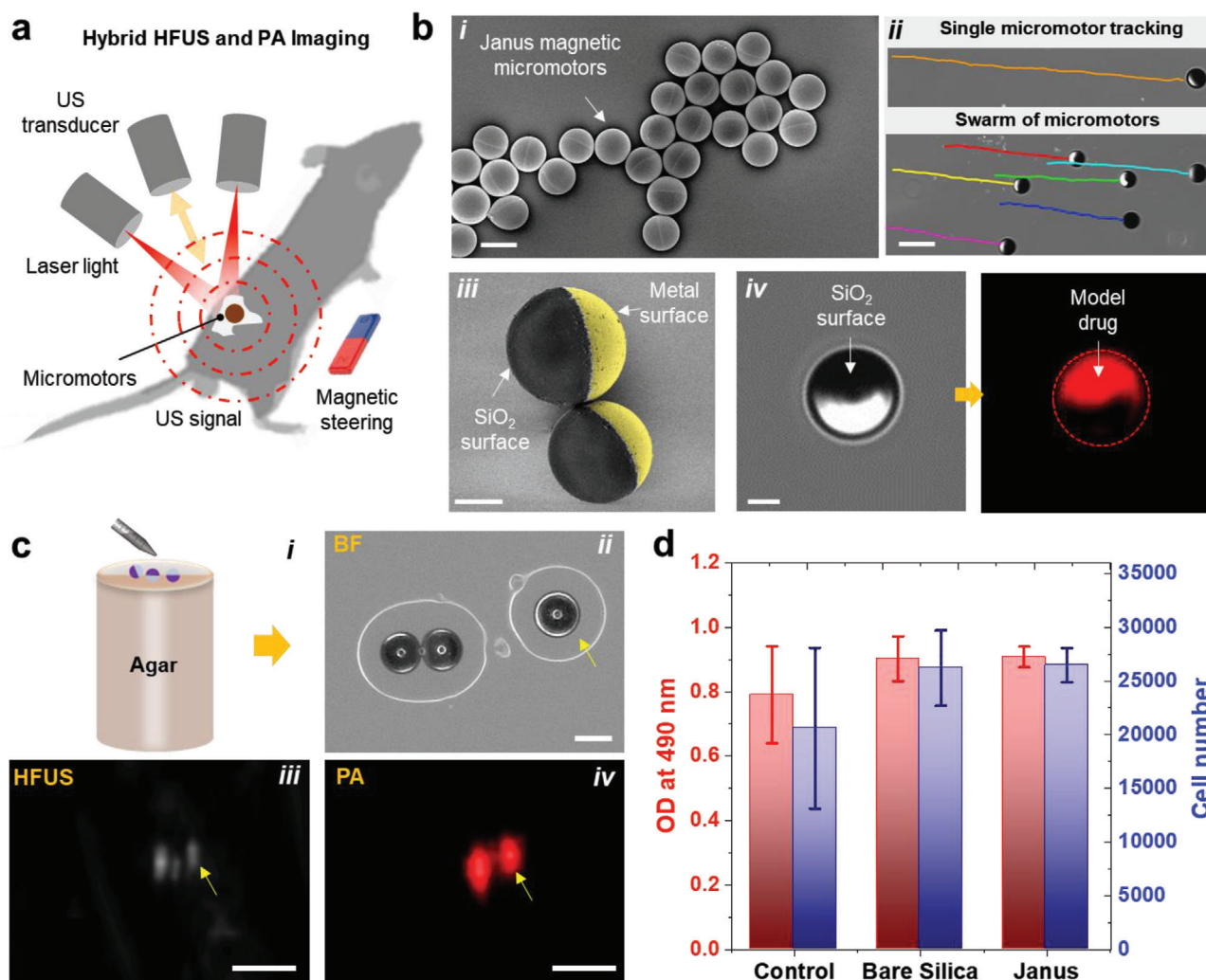


Figure 1. Fabrication and characterization of magnetically driven micromotors. a) Schematic showing the working principle of the employed hybrid HFUS and PA imaging technique. b) Fabrication and functionalization of the micromotors: i) drop-casted SiO₂ particles ($\varnothing = 100 \mu\text{m}$) half-coated with metal layers (10 nm Ti, 50 nm Fe, and 10 nm Ti) using electron beam deposition. Scale bar: 100 μm . ii) Optical tracking of single and swarm of moving micromotors. Scale bar: 200 μm . iii) Pseudo-colored SEM image of two half-coated micromotors and iv) BF and fluorescence images of the functionalized micromotors with a model drug (DOX). Scale bar for iii,iv) 40 μm . c), i) Schematic of an agarose phantom containing the micromotors. Comparison between ii) BF, iii) HFUS, and iv) PA images of single micromotors. Scale bar for BF: 100 μm . These images were acquired at 800 nm, where the fluence was set below the MPE limit of 20 mJ cm⁻². Scale bar for HFUS and PA: 1 mm. d) MTS assay showing cell viability of MSCs after being co-cultured with bare SiO₂ and metal-coated particles to test the cytotoxicity of the employed materials. The control group proceeded without any particles. Each error bar denotes the \pm SD from three replicates ($n = 3$).

2.2. Tracking of Single Micromotors in Phantom and Ex Vivo Tissue

To visualize the micromotors dynamically, the following experiments were conducted in both tubing phantom and ex vivo tissues. For the tubing phantom setup, commercially available methacrylate support (Vevo Phantom, FUJIFILM VisualSonics, the Netherlands) was used to mount transparent intravascular polyurethane (IPU) tubes (inner diameter $\approx 380 \mu\text{m}$ and outer diameter $\approx 840 \mu\text{m}$, SAI Infusion Technologies, USA). The micromotors were inserted into the tube and immersed in the phantom chamber containing DI water for better acoustic coupling (Figure 2a). After the PAI acquisition, the spectral characteristics of the samples were recorded. 3D single-wavelength (800 nm)

imaging was also performed using a 2D stepper-motor and a linear translation of the transducer over the IPU tubing. For control experiments, another tube was mounted with a saline solution. All PA measurements were performed at a gain of 40 dB.

US image quality is influenced by the medium through which sound travels from the transducer. Material choice is a crucial factor in US imaging to match the speed of sound and to avoid undesired artifacts. Thus, the materials must possess low attenuation, meaning that acoustic waves can reach the target (micromotor) and return. The material should also exhibit low backscattering between the micromotor and the transducer. The ratio of the micromotor reflection intensity to backscattering intensity is chosen as a relative figure-of-merit to determine the material performance.^[41] The IPU tubing features low attenuation

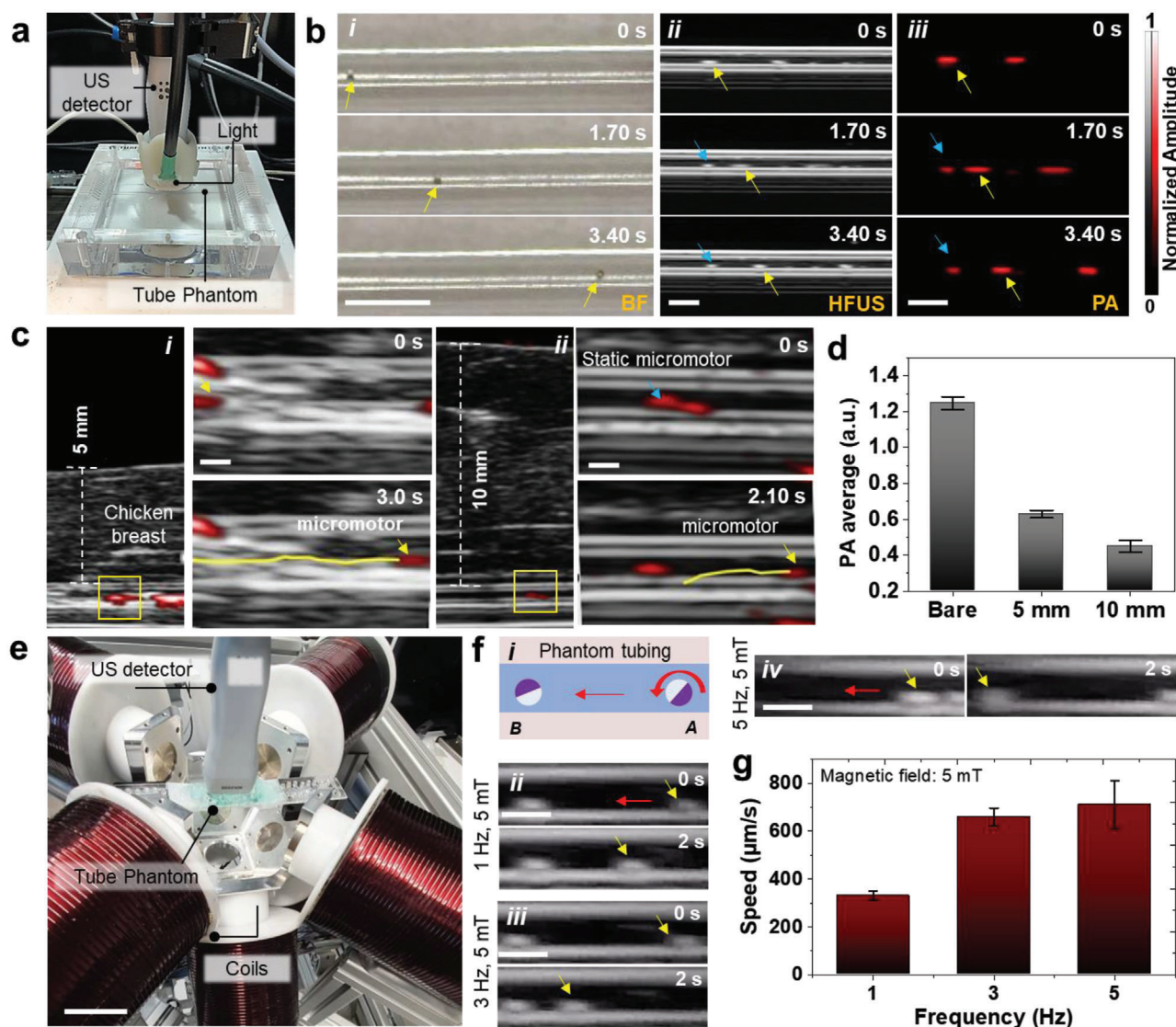


Figure 2. Tracking of single micromotors in phantom and ex vivo chicken tissues. a) Phantom chamber with tubing immersed in a water bath with HFUS-PA detector on top of it for real-time tracking of moving micromotors. b) Time-lapse images of a 100 μm moving micromotor in i) BF, ii) HFUS, and iii) PA modes. Yellow arrows show the single-moving micromotors. Blue arrows point at static microstructures and are used as reference points. Scale bar: 1 mm. c) Time-lapse images of a moving micromotor below i) 5 mm and ii) 10 mm breast chicken tissue. Scale bar: 500 μm . d) PA signal amplitude of single micromotors with comparable ROIs below 5 and 10 mm thick tissue, which decreases with increased penetration depth. e) Integrated imaging and magnetic actuation setup. Scale bar: 4 cm. f, i) Schematic and ii–iv) controlled actuation of single moving micromotor inside the phantom tubing at 5 mT and varying frequencies (1, 3, and 5 Hz). Scale bar: 1 mm. g) The relationship between the micromotor speed and the applied frequency at a constant magnetic field strength. The magnetic field value was set to 5 mT and the frequency was adjusted (from 1 to 5 Hz). Each error bar denotes the \pm SD from three replicates ($n = 3$).

and low front surface backscatter that provides a better HFUS contrast making it possible to visualize single moving micromotors inside this tube phantom. The dynamic tracking of a single micromotor is shown in time-lapse images from 0 to 3.40 s (Figure 2bi–iii), comparing BF, HFUS, and PA imaging modes (Videos S3 and S4, Supporting Information). Blue arrows show the position of static micromotors (stuck on the tube walls) while the yellow arrows correspond to the single moving micromotor. The overlaid HFUS-PA video shows a single micromotor moving forward and backward with clear localization within the phantom tube (Video S4, Supporting Information).

This dual feature is useful in deep tissue imaging where US provides tissue background morphology while PA maintains high contrast of the micromotor material's properties. The measurement was performed with a position-fixed high-frequency transducer (21 MHz) to avoid image distortion.

To visualize the micromotors underneath biological tissues, we employed chicken breast from a local store, with an ≈ 5 and 10 mm thickness (measured with a Vernier scale). The IPU phantom tubing containing the micromotors was placed in between two layers of chicken breast tissue (Figure S4, Supporting Information) for the consequent measurements. The US gel was

applied between the detector surface and the top of the tissue to match the acoustic impedance for efficient signal transfer. HFUS mode generated a structural image, suitable to identify the tubing structure, and the PA system was used to monitor the displacement of the micromotors, by detecting their light absorption characteristics. Both images were acquired in real-time during external magnetic steering. The locomotion of a single micromotor was tracked under 5 and 10 mm thick tissue samples and it was possible to display overlaid HFUS and PA images as shown in time-lapse images (Figure 2ci,ii and Videos S5 and S6, Supporting Information). The corresponding PA amplitude values of the micromotors are shown in Figure 2d. The micromotors exhibited decreased PA intensity when increasing the tissue thickness due to pronounced scattering of the excitation light in deep tissues.

To actuate the micromotors in a controlled manner, a setup consisting of an integrated coil setup and the imaging system was implemented (Figure 2e). The set of coils produces fields up to 50 mT in a frequency range from 0 to 200 Hz and gradients of up to 2 T m^{-1} at 10 Hz. In this experiment, we applied a field strength of 5 mT at a frequency range between 1 and 5 Hz, to steer a single micromotor in a narrow channel (Video S7, Supporting Information, and Figure 2fi–iv). The speed of the micromotor increased by adjusting the frequency as shown in Figure 2g.

2.3. Monitoring of Swimming Micromotors in Bladder and Uterus

The following *in vivo* HFUS and PA experiments were performed under the animal handling license No. DVS06, hold by the co-authors of FUJIFILM VisualSonics, the Netherlands, ensuring the biocompatibility nature of the employed materials. This study was conducted using the same equipment and imaging settings as those for phantoms or *ex vivo* experiments mentioned above. The micromotors were injected into the bladder and uterus of 12-week old mice (details in the Experimental Section). We selected the bladder and uterus cavity as sites of injection to allow enough room for the free-swimming of the micromotors. The bladder is a hollow soft organ that serves as a reservoir for the storage and periodic release of urine, with areal dimensions of $\approx 5.50 \times 6.0 \text{ mm}^2$ as shown in the 2D US image (Figure S5, Supporting Information). Under anesthesia, the mouse bladder was catheterized by following standard safety guidelines and protocols.^[42] Before starting the experiment, the physiological parameters of the mouse were monitored (Figure S6 and Video S8, Supporting Information). First, the micromotors were collected (15–25 in $\approx 20 \mu\text{L}$ phosphate buffered saline (PBS)) in a catheter and then inserted into the bladder. The catheter was inserted through the urethra of an anesthetized mouse (Figure 3a) while being monitored *in vivo* as shown in the 3D US reconstructed image (Figure 3b). After reaching the entrance of the bladder, the micromotors were released gradually into the bladder cavity. The overlaid HFUS and PA image in Figure 3c shows the micromotors near the catheter edge before and after release. PA signal (red spot) highlights the presence of a swarm of micromotors being ejected from the catheter, while US image shows the anatomy of the organ of operation. After release, the micromotors started to move down in the urinal cavity and it was possible to visualize the micromotors from few to swarm of them (Video S9, Supporting

Information). Time-lapse HFUS and PA images show the swimming behavior of micromotors in urinal fluid from top to bottom surface of the bladder for 2.50 s (Figure 3d) and the falling velocity of a cluster of micromotors in the bladder was estimated to be $\approx 1250 \mu\text{m s}^{-1}$ (in the current experiment). Finally, the whole swarm of micromotors at the bottom of the bladder was manipulated by using an external magnet (Videos S10, Supporting Information). The upward displacement of the whole swarm centroid was estimated to be $\approx 3.5 \text{ mm}$ (in the current experiment) after a time interval of $\approx 8 \text{ s}$ and the dimension of the moving cluster was estimated to be between 2 and 3 mm wide (Figure 3e). The upward speed of the swarm was $\approx 480 \mu\text{m s}^{-1}$ after time travel of 7 s and as expected, the speed of the cluster in opposite direction (upward motion) was slower than the downward motion as the gravitational force was dominant over the drag force (with no applied magnetic field). The speed of a single or swarm of micromotors also depends on the strength of the applied field at the evaluated distance from the micromotor position. In this experiment, an estimated magnetic field gradient of $\approx 220 \text{ mT cm}^{-1}$ was applied. To effectively control the micromotors *in vivo*, we employed a magnetic field gradient due to higher magnetic field strength. There is still further optimization required to improve the magnetic field strength with the proposed setup for implementing rotating magnetic fields.

Apart from the bladder, we also evaluated the micromotors imaging in the mouse uterus. In this experiment, the phantom tubing (containing a single micromotor) was inserted into the *ex vivo* uterine horn and fixed with sticking glue on the imaging surface (Figure 4a). The precise steering of a single rotating micromotor was captured under a rotating magnetic field of 5 mT and 5 Hz (Figure 4b and Video S11, Supporting Information). In this setup, after preparing the *ex vivo* tissue, the trajectory of a single micromotor through the tubing was precisely controlled in a fourth and backward fashion from 0 to 25 s.

After evaluating their tracking under *ex vivo* tissues, the micromotors were inserted into the mouse uterus *in vivo* as depicted in a schematic (Figure 4c). The catheter was inserted via the vagina and cervix into the mouse uterus cavity by following previous safety guidelines.^[42] In this experiment, we investigated the smallest detectable feature size of the micromotors in the uterus by injecting a controlled number of micromotors. By employing US imaging, it was possible to precisely locate the catheter tip at the opening of the uterus cavity before micromotors insertion (Figure 4d). Ultimately, it was possible to deliver approximately two to three micromotors in the mouse uterus from the catheter needle. Then, one of the micromotors was steered in real-time over a trajectory of $\approx 950 \mu\text{m}$ (Video S12, Supporting Information). Time-lapse HFUS and PA images showed the moving micromotor from one position to another for 3.60 s (Figure 4e). The resulted images comprise PA amplitude values of the uterus cavity with and without micromotors (control) by choosing comparable ROIs (Figure 4f).

HFUS images have speckle patterns from the background tissues which makes it challenging to identify the micromotors. The tracked micromotor was visible in both HFUS and PA modes; however, it is clear that HFUS provided better visualization of the catheter entrance and the surrounding uterus anatomic features, while PA facilitated the discrimination of the light-absorbing micromotors from the surrounding environment, offering a high

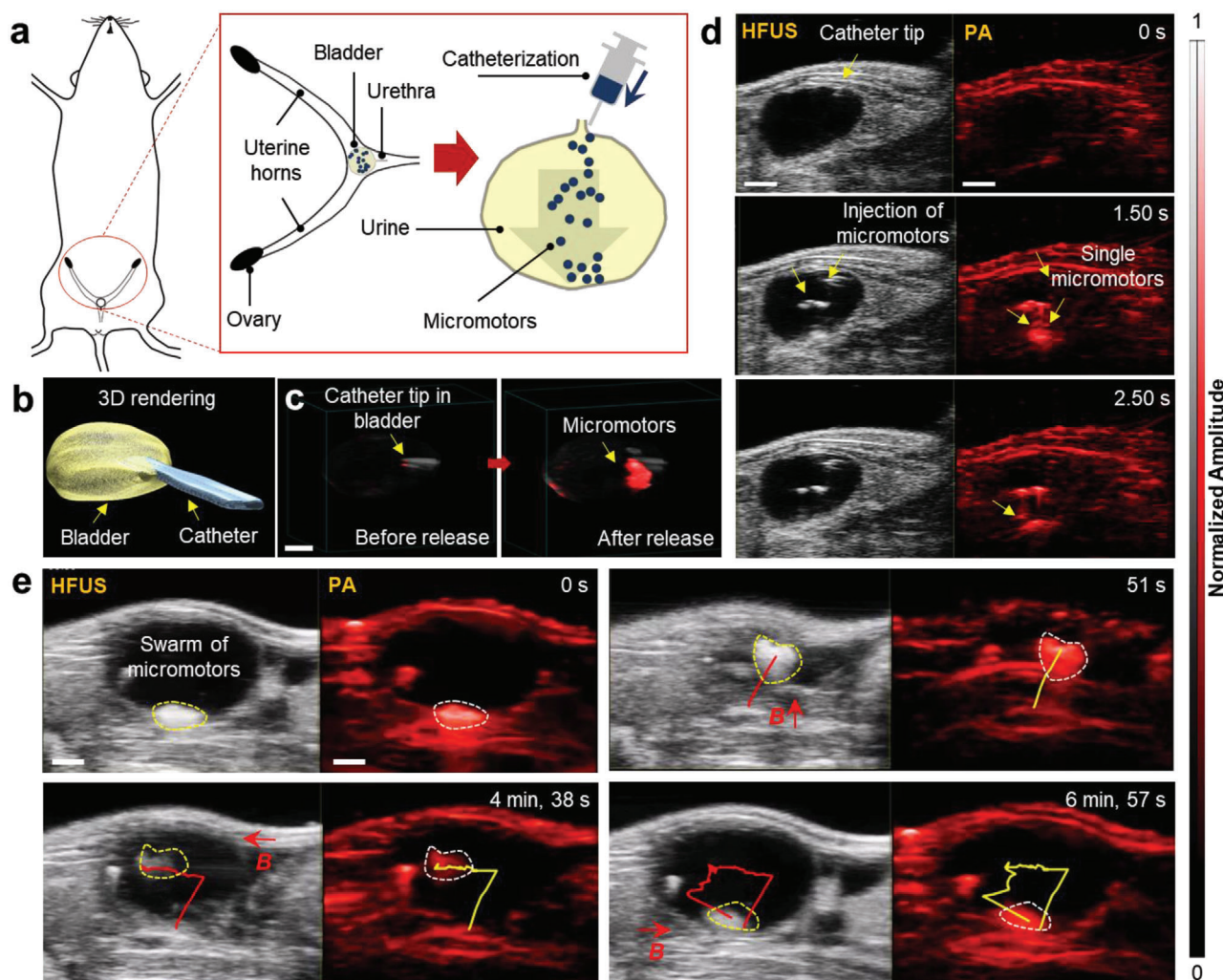


Figure 3. HFUS and PA imaging of a single and swarm of micromotors swimming inside a mouse bladder. a) Schematic showing the position of the bladder. b) 3D reconstruction of the bladder with the inserted catheter, after performing the catheterization via real-time US feedback. c) HFUS and PA overlaid images showing the location of the catheter tip, before and after releasing the micromotors. d) Dual HFUS and PA time-lapse images of swimming and free-falling micromotors for 2.50 s. The micromotors migrate downward after being released from the catheter tip individually and then accumulate at the bottom surface. Scale bar, 1 mm. e) A swarm of swimming micromotors under the actuation of a magnetic field gradient of $\approx 220 \text{ mT cm}^{-1}$. The dimension of this moving cluster was $\approx 2\text{--}3 \text{ mm}$ wide. Scale bar: 2 mm.

signal-to-noise ratio (SNR). The employed micromotors and the here-evaluated imaging system is appealing for the supervised cargo delivery toward urinary tract diseases, e.g., urethral stenosis, bladder cancer, or infection, or toward *in vivo* assisted fertilization, where similar engineered parts can be used for instance to guide or transport sperm,^[4,10] and zygotes^[43] in the reproductive tract.

The PAI also offers the advantage of multiplexed imaging or spectral unmixing to distinguish light-absorbing signals coming from the different organic and inorganic components present in the field of view.^[44] The multi-wavelength mode takes advantage of the tunability of the pulsed laser source to acquire PA data at multiple wavelengths in 2D and 3D for automated post-processing, obtaining a unique spectrum. Such specific spectral capacity of PAI offers specific detection of endogenous molecules like oxygenated (oxy-Hb) and deoxygenated hemoglobin (deoxy-

Hb), among others.^[30] The first step is to image the target (micromotors, oxy- and deoxy-Hb or other employed materials) at multiple wavelengths. Then the spectral unmixing algorithm is applied, generating separate images based on the contrast obtained from the different absorber materials (endogenous or exogenous). Thus, when merging the independent images, one can obtain the distribution of oxy- or deoxy-hemoglobin as well as of the present micromotors marked according to their absorption properties.

In this experiment, 10 μL of micromotors suspended in PBS were injected into the hind limb (popliteal lymph node fat pad), followed by the PA multi-wavelength measurement in the range of 680–970 nm with a step size of 5 nm. The obtained signals were then spectrally unmixed to discriminate the PA signal of the injected micromotors from the surrounding tissue chromophores. 3D reconstruction of the target site demonstrates the

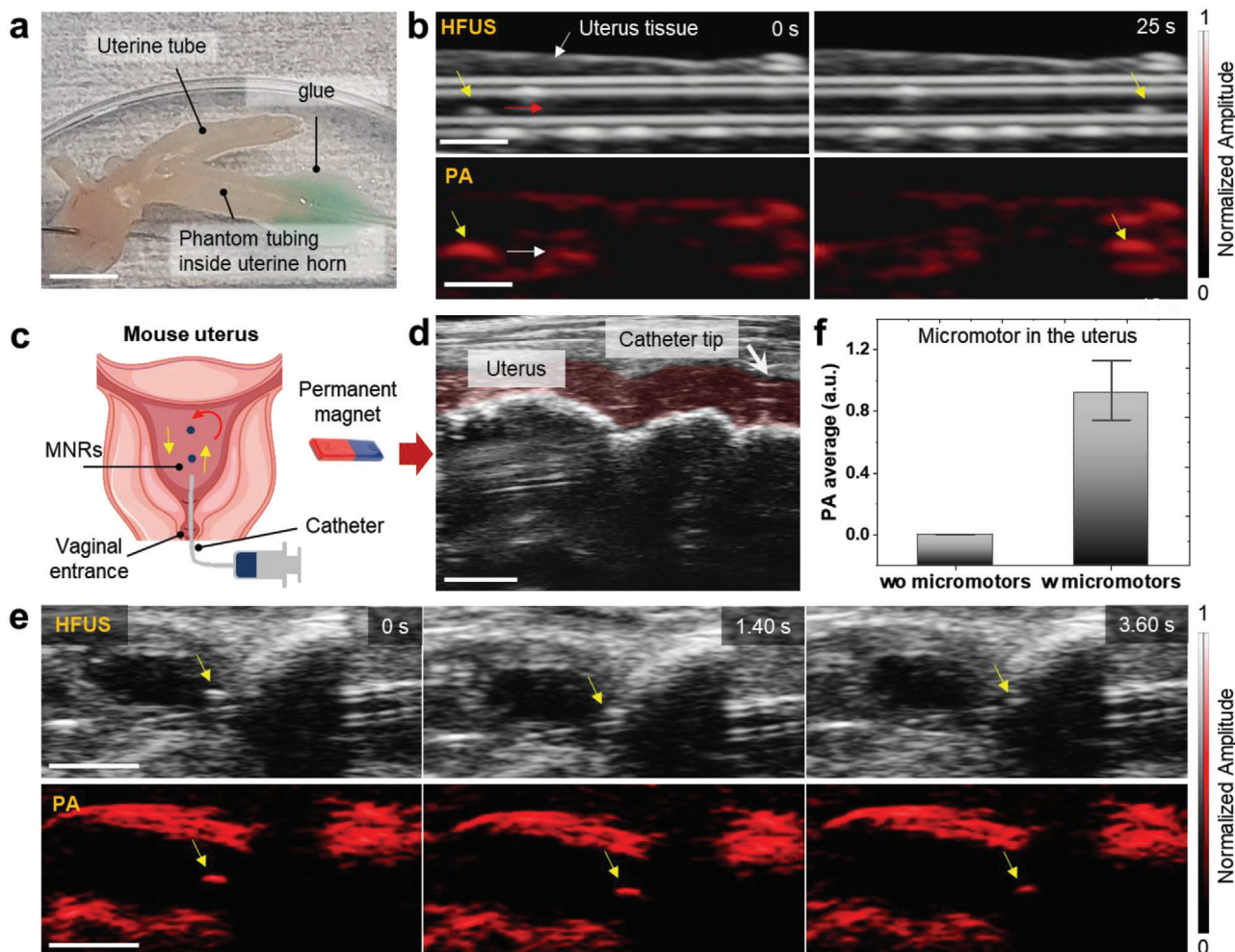


Figure 4. HFUS and PA imaging of micromotors in ex vivo and in vivo uterus cavity. a) The phantom tubing (with single micromotor) was inserted in an ex vivo uterine horn and glued to avoid liquid leakage. Scale bar: 5 mm. b) Precise magnetic control of a single micromotor into an ex vivo uterine horn under rotating magnetic fields (5 mT and 5 Hz) for 0 to 25 s. Scale bar: 1 mm. c) Schematic showing the insertion of the catheter into the uterus body through the vagina and moving micromotors by applying an external magnetic field. d) Real-time HFUS feedback of positioning the catheter in the mouse's uterus. The red-shaded area indicates the uterus channel. Scale bar: 2 mm. e) Time-lapse images of single moving micromotors (yellow arrows show the position of moving micromotor). Scale bar: 2 mm. f) PA amplitude values extracted from the captured PA images of a single moving micromotor, compared to the control (uterus location where no micromotors were visible "wo micromotor").

spectral behavior of the injected micromotors (yellow color) and the chromophores present in blood, i.e., oxy-Hb, deoxy-Hb (Figure S7, Supporting Information). The PA amplitude values of the micromotors were extracted from the captured PA images and then calibrated with the previously measured optical absorption of hemoglobin. 3D multiplexing PA scans have allowed investigating the biodistribution of the injected micromotors in vivo which in turn can be used to target specific body organs to perform a certain medical task. This is particularly important when the micromotors are injected within the tissue where there is not good contrast.

2.4. Potential Biomedical Application

As reported previously in the literature, metal-coated particles have been shown as drug carriers, propelled either by bacteria,

physical fields or by chemical reactions to target cancer cells in vitro,^[26,45,46] with a loading mechanism ranging from physical absorption/adsorption to more sophisticated stimuli-responsive delivery triggers. In this section, as a potential application of employed magnetically driven micromotors, we loaded DOX, an anticancer drug, onto the micromotor's surface and evaluated its therapeutic effect over time (details in the Experimental Section). The experiments were performed under physiological conditions (at 37 °C). As DOX is autofluorescent (excitation wavelength: 470 nm and emission wavelength: 580 nm), we recorded images over 24 h, maintaining a constant exposure time (Figure 5a,b). After that, we carried out a cargo-delivery experiment, by first steering the micromotors under rotating magnetic fields nearby a 2D culture cancer cells (Figure 5ci-iv) and then by monitoring the drug release by diffusion under time-lapse fluorescence microscopy. The cell-killing efficacy of the DOX-loaded micromotors was qualitatively investigated by co-incubating DOX-loaded

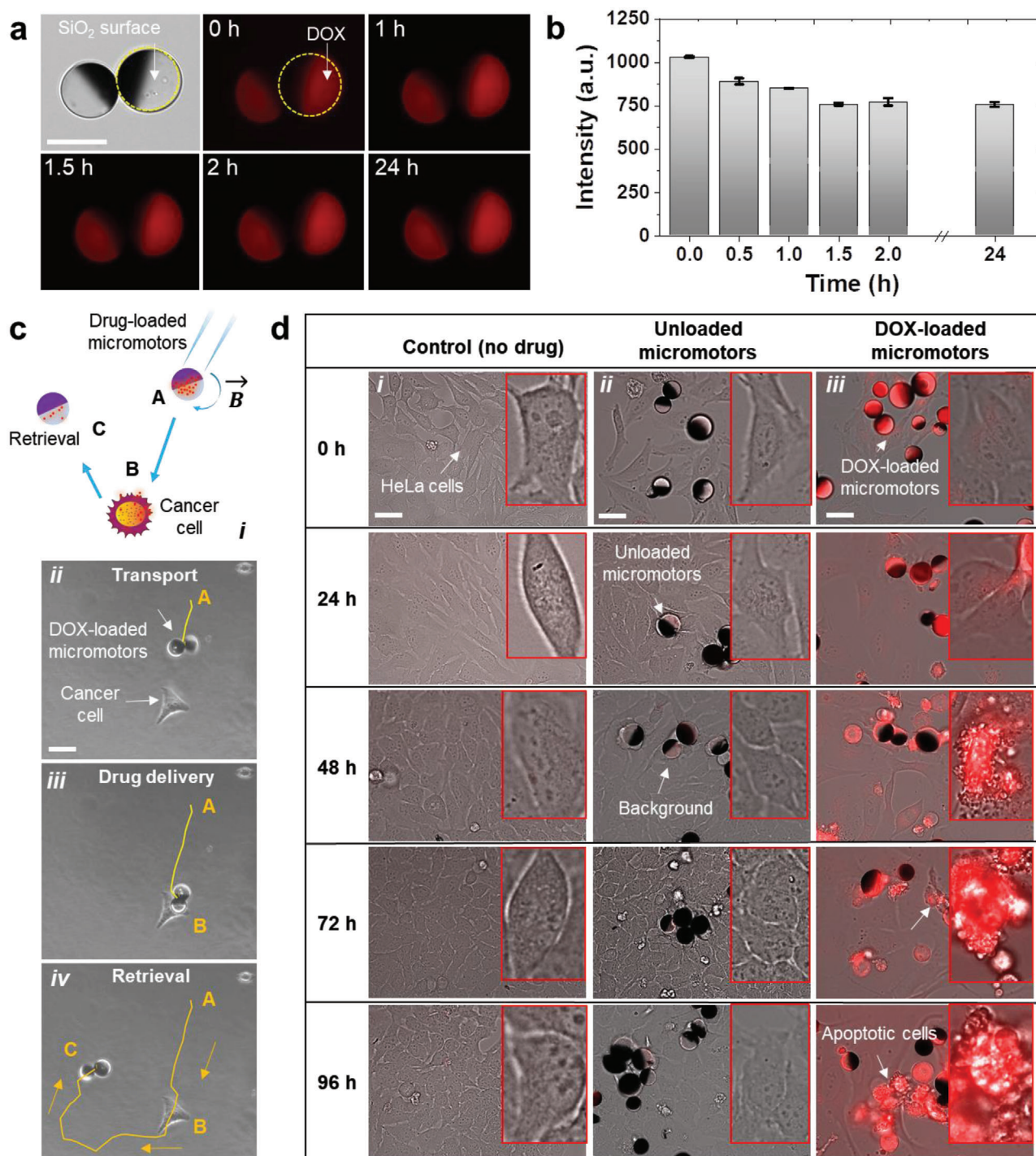


Figure 5. Study of DOX-loaded micromotors functionality. a) Fluorescence images of DOX-loaded micromotors over 24 h, Scale bar: 20 μm . b) Fluorescence intensity of the drug-loaded micromotors. c) Schematic showing the transport of drug-loaded micromotors from position A to the target HeLa cell (position B). After releasing the drug, the micromotor can be retrieved by applying an inverse rotating magnetic field, and be transported to the desired location (position C). Optical images show the complete trajectory indicating i) transport, ii) drug-release, and iii) retrieval of a micromotor. Scale bar: 20 μm . d) Time-lapse fluorescence images showing DOX diffusion by the transported micromotors onto the 2D cell culture. Images were taken at an excitation wavelength of 470 nm and an emission wavelength of 580 nm. Overlaid BF and fluorescence images captured from 0 to 96 h for each group: i) control sample, ii) with unloaded micromotors, and iii) with drug-loaded micromotors. Scale bar: 20 μm . HeLa cells were cultured in a coverslip in a cell culture medium and grown for 3 d in the incubator at 37 $^\circ\text{C}$ and 5% CO_2 , cell count = 5×10^4 for each sample.

micromotors ($\approx 10 \mu\text{L}$ solution) with HeLa cells (5×10^4 for each sample) over 96 h. HeLa cells without any drug as well as HeLa cells with unloaded micromotors were chosen as control experiments (see details in the Experimental Section). Overlaid BF and fluorescence images were captured from 0 to 96 h for each sample (Figure 5di–iii). As expected, unloaded micromotors showed no cell killing ability while drug-loaded micromotors indeed induced cell apoptosis, which can be seen by a change in cell size and morphology over time (Figure 5diii).

To check the stability of the drug-loaded micromotors under PAI, the absorption signal of the drug should be detectable in the NIR range. Since DOX has a signal intensity in the visible range (peak at $\approx 580 \text{ nm}$), it was not possible to monitor it via PAI. However, as a proof of concept we employed an IR absorbing cargo, an food and drug administration (FDA) approved contrast agent called indocyanine green (ICG). ICG possesses a unique absorption peak at 880 nm which facilitates the visualization via PAI, with negligible artifacts arising from autofluorescence or surrounding tissues deep in the body. It can be used for instance to label the therapeutic cargo. Thus, we functionalized the micromotors with ICG and monitored their cargo-release under scattering tissues (Figure S8, Supporting Information). Future studies will be oriented to functionalize drugs with NIR reporters or employ NIR-absorbing genes which can be used not only for tumor labeling but also for therapy.^[47] The monitoring of drug release can also be implemented for sophisticated drug carriers in which the release of the drug can be triggered by endogenous or exogenous stimuli,^[48] as in a recently reported work, where the NIR light irradiation by PAI was sufficient to disintegrate the capsules to deliver the micromotors in the stomach of a mouse,^[39] or for triggering the drug release for treating sub-skin pathogenic bacterial infections via photothermal therapy (heating of a bacterial site up to $54 \text{ }^\circ\text{C}$).^[24]

3. Conclusions

Hybrid imaging techniques in particular when combining anatomical and functional operating modes provide superior advantages for translational medicine and biomedical studies. For example, a PET-CT system offers the combination of high-resolution anatomical information with intravital molecular data.^[49] Similarly, hybrid fluorescence molecular tomography and X-ray CT offer improved penetration depth.^[50] In the present study, we implemented a dual HFUS and PA imaging system to carry out anatomical and functional imaging of swimming micromotors deep in the bladder and uterus of a mice model with the envisioned application of supervised cargo delivery.

This technique provided from one side the volumetric US image and on the other side the PA distribution map of hemoglobins in the region of interest and resolved the micromotors from the signal of the surrounding tissues. HFUS was suitable for the real-time monitoring of the catheterization and localization of the target organ to deliver single or swarms of micromotors. Likewise, PAI allowed the reliable monitoring of the injected micromotors due to their IR absorption properties, discriminating them from the signal of endogenous chromophores. Additionally, the integrated magnetic coil setup provided open-loop control of magnetic micromotors while being simultaneously monitored via HFUS-PA imaging. Moreover, multispectral

imaging was employed to extract the specific absorption spectrum from each of the present entities (MNRs and biological tissues), being of crucial importance when operating in biological environments which contain a variety of chromophores or absorbing molecules that hinder the MNRs signal. In the end, DOX-loaded micromotors were investigated to induce local cancer cell apoptosis and a potential drug label called ICG, which absorbs light in the NIR was used to demonstrate the possibility to monitor drug release by the micromotor under scattering tissues over time.

So far, the here reported experiments have been performed in ex vivo tissues and living mice. However, to translate this technology to humans and despite all the ethical discussions around the employment of medical micromotors which will arise in the next years, some technical limitations need to be solved such as the penetration depth (so far $\approx 2 \text{ cm}$, with the micrometric resolution has been possible), but going beyond this limit will compromise the spatial and temporal resolution. Biodegradability is another prerequisite and the employed materials should be non-toxic after interaction with human cells.^[51] There have been few attempts of biocompatible micromotors for drug-delivery applications^[39,52,53] and eventually, the micromotors should clear the body after performing an assigned task without any diverse effects.

In summary, this work settles the methodology to perform real-time control of magnetically driven micromotors under scattering tissues, employing dual anatomical and functional imaging techniques, for a variety of medical-relevant applications.

4. Experimental Section

Fabrication of the Micromotors: The micromotors were constructed using a drop-casting method with subsequent thin metal layer deposition as described previously.^[26] First, glass substrates ($22 \times 22 \text{ mm}^2$) were rinsed and ultrasonicated (Elmasonic, Elma Schmidbauer GmbH) in acetone and isopropanol for 3 min each and finally dried in a stream of N_2 . The substrates were exposed with oxygen plasma (Diener electronics), leading to the removal of impurities and contaminants from the glass surface, to obtain clean and hydrophilic substrates. Afterward, a monolayer of micro-sized ($\varnothing = 100 \mu\text{m}$, Corpuscular Inc. USA) silicon dioxide (SiO_2) particles was assembled. In detail, SiO_2 particles were washed with methanol and centrifuged for 1 min to remove supernatant and then again mixed with methanol and vortexed (Vortex mixer, VWR) before usage. Silica particles were mixed thoroughly in methanol and $\approx 20\text{--}25 \mu\text{L}$ of the particle-solvent solution was drop casted on the edge of a pre-plasma treated glass slide. The glass slide was adjusted at an angle to allow the spreading of silica particles over the entire glass coverslip, making a homogeneous monolayer of silica particles. The microarrays were randomly formed in the direction of solvent evaporation. The resulted monolayer was dried at room temperature.^[26] After drying, the samples were half-coated with Ti (10 nm), Fe (50 nm), and Ti (10 nm) of high purity (99.995%) by electron beam physical vapor deposition (e-beam evaporator, Plassys MEB550S) at a deposition rate between 0.5 and 1.0 \AA s^{-1} . Fe layer was evaporated for magnetic guidance and Ti was chosen for biocompatibility.

SEM and optical microscopy were performed for the characterization of the prepared micromotors. SEM (Zeiss Nvision 40, Carl Zeiss Microscopy GmbH) was performed by coating the sample with $\approx 10 \text{ nm}$ Pt to make the specimen conductive and to avoid charging effects during imaging. Bright-field microscopy was performed using an optical microscope (Zeiss Microscopy GmbH) equipped with 5x, 10x, and 20x objectives.

Fabrication of Agarose Phantoms: Agarose is a cost-effective bacteriological powder that, when dissolved in water, remains in a gelatinous

state at ambient temperature after being warmed up. Agarose phantoms mimic soft tissues and some preparation techniques are described in refs. [54–56]. Briefly, 100 mL DI water was heated at 300 °C and then 1.50 g of agarose was slowly added and gently mixed forming a homogeneous solution. Afterward, 6 mL soya milk (Alpro, UK) was added to include tissue-mimicking scattering. After adding milk, the solution was mixed and 5 mL of this mixture was poured into a petri dish. The solution was left to cool down at room temperature for ≈ 60 min to solidify.

Ex Vivo Tissue Setup: Chicken breast samples were purchased from a local store and used with thicknesses of 5 and 10 mm. The IPU tubing was filled with the micromotors suspended in PBS 1X and then placed between two 5 mm thick tissue samples. The process was repeated for 10 mm thick tissues afterward. To ensure uniform distribution of thickness and prevent drying, the thickness of the tissue samples was measured using a digital Vernier Caliper. The tissues containing micromotors were then placed on an imaging chamber grid for tracking measurements.

In Vivo Mice Handling: The in vivo mice experiments were conducted at the FUJIFILM VisualSonics laboratory in Amsterdam. The animal protocols used in this work were appraised and approved by the Committee on Ethics in the Use of Animals, the Netherlands (Protocol AVD2450020173644). They conform with federation of european laboratory animal science associations (FELASA) guidelines and the National Law for Laboratory Animal Experimentation (Law No. 18.611). The experiments were performed by using the same equipment used for the phantom studies. 12 weeks old mice were used for in vivo imaging in the bladder and uterus. All mice were anesthetized using isoflurane, at a concentration of 1.5–2%. O₂ flow (1–2 mL min⁻¹ maintenance) mixed with isoflurane. For optimized coupling of the ultrasound gel the rodent fur needed to be removed using commercially available depilation cream. For 3D multiplexing imaging, an institute for cancer research (ICR) CD-1 ± 25 g (an albino outbred strain of mouse model) female mouse was injected with a 10 μ L mixture of PBS 1X and micromotors into the hind limb (popliteal lymph node fat pad). 3D PA multiwavelength was applied to automatically unmix the injected micromotors. PA multispectral imaging distinguished the difference in optical signals related to the micromotors in 2D and 3D for subsequent postprocessing.

HFUS and PA Imaging of the Micromotors: PA measurements were carried out by using the Vevo-LAZR X (FUJIFILM VisualSonics, the Netherlands) system, a multimodal platform that allows the simultaneous imaging of high-resolution ultrasound and photoacoustics. The system was equipped with a linear array ultrasound transducer at a central frequency of 21 MHz (MX 250, FUJIFILM VisualSonics, the Netherlands) and fiber optic bundles on either side of the transducer for illumination. The fiber bundle was coupled to a tunable Neodymium-doped yttrium aluminum garnet (Nd:YAG) laser (680 to 970 nm) with a 20 Hz repetition rate and the signals were collected by the 256-element linear array transducer. The pulsed laser generated a wavelength-tunable pulsed beam (680–970 nm) which was delivered by a bifurcated fiber bundle integrated with US transducer. Both HFUS and PA signals were collected and reconstructed using on-board software. For single pulse excitation, the PA images were acquired at an excitation wavelength of 800 nm (with in-plane axial (75 μ m) and temporal (5–20 fps) resolution. The same protocol was applicable for in vivo imaging in mice bladder and uterus.

Drug Loading (ICG or DOX): The magnetically driven micromotors were loaded with an anti-cancer drug (DOX), which is widely approved for cancer therapy, and a model drug (indocyanine, ICG). ICG is an FDA-approved contrast agent for use in humans and was employed for this experiment due to its unique absorption peak at 880 nm. The micromotors were functionalized by overnight incubation in an ICG or DOX using the same protocol. ICG or DOX solution was prepared with a concentration of 100 μ g mL⁻¹ and then mixed with the micromotor solution with PBS (≈ 10 μ L). The mixture was covered with aluminum foil and incubated for 24 h.

To evaluate the loading of the DOX micromotors, fluorescence microscopy was used to track a single micromotor with an excitation wavelength of 470 nm. It was possible to distinguish drug-loaded micromotors from unloaded (control) ones using fluorescence microscopy. DOX possesses an intrinsic fluorescence with an emission peak at around 600 nm

(Figure 1biv). It shows the potential of using micromotors as a drug-carriers.

HeLa Cell Killing Experiment: The DOX-loaded micromotors were co-incubated with HeLa cells for an effective cell-killing experiment. HeLa cells are derived from cervical cancer cells and were cultured in a cell culture medium (Dulbecco's modified Eagle medium 5671, 10% fetal calf serum, 1% penicillin/streptomycin (Pen/Strep), 1% L-glutamine). Before cell culture, the coverslips were first cleaned in an ultrasonic bath with acetone and isopropanol and afterward dried with an N₂ gun. To improve the cell adhesion to the surface of the coverslip, the surface was functionalized with fibronectin using 1-Ethyl-3-(3-dimethylaminopropyl)carbodiimide (EDC) and N-hydroxysuccinimide (NHS) chemistry.

The cell-killing efficacy of the DOX drug was investigated by co-incubation of DOX-loaded micromotors (≈ 10 μ L solution) with HeLa cells (5×10^4 for each sample). HeLa cells without any drug were cultured as control experiments in a coverslip in a cell culture medium (3 mL solution) and grown for 3 d at 37 °C and 5% CO₂. Afterward, the DOX solution was prepared with a concentration of 100 μ g mL⁻¹ in cell medium and mixed with half-metal coated particles. In the last step, the DOX-loaded micromotors were co-incubated with HeLa cells and fluorescence imaging was performed over 96 h. Red fluorescence showed the intensity, indicating the presence of DOX drug in the particles and the surrounding HeLa cells. After 96 h, the size and shape of the HeLa cells were changed due to the drug-induced cell death and the drug was successfully transferred to the targeted HeLa cells for effective cell-killing.

Statistical Analysis: Dual HFUS and PA raw data were treated with Vevo Lab analysis software (FUJIFILM VisualSonics, the Netherlands). The repeated measurements were averaged to obtain general analysis for the speed of the micromotors. Origin 2019 and ImageJ were used for the analysis of the experimental data. The sample size ($n = 3$) was chosen for three independent experiments with at least ten analyzed samples. This was expressed by the SD of the mean value of the replicates. Particle size distribution of SiO₂ microparticles ($n = 260$) was performed with ImageJ and then further analyzed with Origin.

Supporting Information

Supporting Information is available from the Wiley Online Library or from the author.

Acknowledgements

This work was supported by the German Research Foundation SPP 1726 “Microswimmers-From Single Particle Motion to Collective Behavior” and for the European Research Council (ERC) under the European Union's Horizon 2020 research and innovation program (Grant Agreement Nos. 835268 and 853609). O.G.S. acknowledges financial support by the Leibniz Program of the German Research Foundation. The authors thank Franziska Hebenstreit for MTS assay and cell-killing experiment and Haifeng Xu for discussion in DOX experiment. The authors also thank Jithin Jose for his comments and discussion in the paper.

Open access funding enabled and organized by Projekt DEAL.

Conflict of Interest

The authors declare no conflict of interest.

Data Availability Statement

Research data are not shared.

Keywords

dual in vivo imaging, medical tracking, micromotors, photoacoustics, ultrasound

Received: July 5, 2021

Revised: July 29, 2021

Published online: August 11, 2021

- [1] B. J. Nelson, I. K. Kaliakatsos, J. J. Abbott, *Annu. Rev. Biomed. Eng.* **2010**, *12*, 55.
- [2] M. Medina-Sánchez, O. G. Schmidt, *Nature* **2017**, *545*, 406.
- [3] G.-Z. Yang, J. Bellingham, P. E. Dupont, P. Fischer, L. Floridi, R. Full, N. Jacobstein, V. Kumar, M. McNutt, R. Merrifield, B. J. Nelson, B. Scassellati, M. Taddeo, R. Taylor, M. Veloso, Z. L. Wang, R. Wood, *Sci. Rob.* **2018**, *3*, eaar7650.
- [4] H. Xu, M. Medina-Sánchez, V. Magdanz, L. Schwarz, F. Hebenstreit, O. G. Schmidt, *ACS Nano* **2018**, *12*, 327.
- [5] R. Fernandes, D. H. Gracias, *Adv. Drug Delivery Rev.* **2012**, *64*, 1579.
- [6] Z. Hosseinidoust, B. Mostaghaci, O. Yasa, B. W. Park, A. V. Singh, M. Sitti, *Adv. Drug Delivery Rev.* **2016**, *106*, 27.
- [7] B. E.-F. de Ávila, P. Angsantikul, J. Li, M. Angel Lopez-Ramirez, D. E. Ramírez-Herrera, S. Thampiwatana, C. Chen, J. Delezuk, R. Samakapiruk, V. Ramez, L. Zhang, J. Wang, *Nat. Commun.* **2017**, *8*, 272.
- [8] S. Yim, E. Gultepe, D. H. Gracias, M. Sitti, *IEEE Trans. Biomed. Eng.* **2014**, *61*, 513.
- [9] I. S. M. Khalil, A. Adel, D. Mahdy, M. M. Micheal, M. Mansour, N. Hamdi, S. Misra, *APL Bioeng.* **2019**, *3*, 026104.
- [10] M. Medina-Sánchez, L. Schwarz, A. K. Meyer, F. Hebenstreit, O. G. Schmidt, *Nano Lett.* **2016**, *16*, 555.
- [11] M. Medina-Sánchez, H. Xu, O. G. Schmidt, *Ther. Delivery* **2018**, *9*, 303.
- [12] M. Guix, S. M. Weiz, O. G. Schmidt, M. Medina-Sánchez, *Part. Part. Syst. Charact.* **2018**, *35*, 1700382.
- [13] A. Chałupniak, E. Morales-Narváez, A. Merkoçi, *Adv. Drug Delivery Rev.* **2015**, *95*, 104.
- [14] L. Schwarz, M. Medina-Sánchez, O. G. Schmidt, *Appl. Phys. Rev.* **2017**, *4*, 031301.
- [15] S. K. Srivastava, G. Clergeaud, T. L. Andresen, A. Boisen, *Adv. Drug Delivery Rev.* **2019**, *138*, 41.
- [16] L. Ricotti, A. Cafarelli, V. Iacovacci, L. Vannozzi, A. Menciassi, *Curr. Nanosci.* **2015**, *11*, 144.
- [17] V. Iacovacci, G. Lucarini, L. Ricotti, P. Dario, P. E. Dupont, A. Menciassi, *Biomed. Microdevices* **2015**, *17*, 63.
- [18] A. Aziz, S. Pane, V. Iacovacci, N. Koukourakis, J. Czarske, O. G. Schmidt, A. Menciassi, M. Medina-Sánchez, *ACS Nano* **2020**, *14*, 10865.
- [19] Q. Wang, L. Zhang, *IEEE Open J. Nanotechnol.* **2020**, *1*, 6.
- [20] I. S. M. Khalil, P. Ferreira, R. Eleutério, C. L. De Korte, S. Misra, in *Proc. IEEE Int. Conf. Rob. Autom.*, IEEE, Piscataway, New Jersey, USA **2014**, pp. 3807–3812.
- [21] O. Felfoul, M. Mohammadi, S. Taherkhani, D. de Lanauze, Y. Z. Xu, D. Loghin, S. Essa, S. Jancik, D. Houle, M. Lafleur, L. Gaboury, M. Tabrizian, N. Kaou, M. Atkin, T. Vuong, G. Batist, N. Beauchemin, D. Radzioch, S. Martel, *Nat. Nanotechnol.* **2016**, *11*, 941.
- [22] D. Vilela, U. Cossío, J. Parmar, A. M. Martínez-Villacorta, V. Gómez-Vallejo, J. Llop, S. Sánchez, *ACS Nano* **2018**, *12*, 1220.
- [23] V. Iacovacci, A. Blanc, H. Huang, L. Ricotti, R. Schibli, A. Menciassi, M. Behe, S. Pané, B. J. Nelson, *Small* **2019**, *15*, 1900709.
- [24] L. Xie, X. Pang, X. Yan, Q. Dai, H. Lin, J. Ye, Y. Cheng, Q. Zhao, X. Ma, X. Zhang, G. Liu, X. Chen, *ACS Nano* **2020**, *14*, 2880.
- [25] A. Servant, F. Qiu, M. Mazza, K. Kostarelos, B. J. Nelson, *Adv. Mater.* **2015**, *27*, 2981.
- [26] A. Aziz, M. Medina-sánchez, N. Koukourakis, J. Wang, R. Kuschmierz, H. Radner, J. W. Czarske, O. G. Schmidt, *Adv. Funct. Mater.* **2019**, *29*, 1905272.
- [27] D. Li, D. Dong, W. Lam, L. Xing, T. Wei, D. Sun, *IEEE Trans. Biomed. Eng.* **2019**, *67*, 2349.
- [28] S. Gigan, *Nat. Photonics* **2017**, *11*, 14.
- [29] V. Ntziachristos, *Nat. Methods* **2010**, *7*, 603.
- [30] A. Taruttis, V. Ntziachristos, *Nat. Photonics* **2015**, *9*, 219.
- [31] M. Omar, J. Aguirre, V. Ntziachristos, *Nat. Biomed. Eng.* **2019**, *3*, 354.
- [32] T. Zhao, A. E. Desjardins, S. Ourselin, T. Vercauteren, W. Xia, *Photoacoustics* **2019**, *16*, 100146.
- [33] P. Beard, *Interface Focus* **2011**, *1*, 602.
- [34] F. M. Mims III, *Optics News* **1980**, *6*, 8.
- [35] A. G. Bell, *Am. J. Sci.* **1880**, *20*, 305.
- [36] A. Aziz, M. Medina-Sánchez, J. Claussen, O. G. Schmidt, *Nano Lett.* **2019**, *19*, 6612.
- [37] A. Aziz, M. Medina-Sánchez, J. Claussen, O. G. Schmidt, *Proc. MARSS 2019: 4th Int. Conf. Manipulation, Autom., Rob. Small Scales*, IEEE, Piscataway, New Jersey, USA **2019**.
- [38] A. Aziz, M. Medina-Sánchez, J. Claussen, O. G. Schmidt, *arXiv* **2019**, arXiv:1907.09264.
- [39] Z. Wu, L. Li, Y. Yang, P. Hu, Y. Li, S.-Y. Yang, L. V. Wang, W. Gao, *Sci. Rob.* **2019**, *4*, eaax0613.
- [40] R. J. Thomas, B. A. Rockwell, W. J. Marshall, R. C. Aldrich, S. A. Zimmerman, R. J. Rockwell, *J. Laser Appl.* **2001**, *13*, 134.
- [41] B. E. Yunker, D. Cordes, A. L. Scherzinger, G. D. Dodd, R. Shandas, Y. Feng, K. S. Hunter, *Med. Phys.* **2013**, *40*, 052905.
- [42] P. A. Oliveira, M. J. Pires, C. Nóbrega, R. Arantes-Rodrigues, A. M. Calado, J. Carrola, M. Ginja, A. Colaço, *Scand. J. Lab. Anim. Sci.* **2009**, *36*, 5.
- [43] L. Schwarz, D. D. Karnaushenko, F. Hebenstreit, R. Naumann, O. G. Schmidt, M. Medina-Sánchez, *Adv. Sci.* **2020**, *7*, 2000843.
- [44] A. A. Oraevsky, *Photoacoustics* **2015**, *3*, 1.
- [45] M. M. Stanton, J. Simmchen, X. Ma, A. Miguel-López, S. Sánchez, *Adv. Mater. Interfaces* **2015**, *3*, 1500505.
- [46] A. C. Hortelão, T. Patiño, A. Perez-Jiménez, À. Blanco, S. Sánchez, *Adv. Funct. Mater.* **2018**, *28*, 1705086.
- [47] J. Lavaud, M. Henry, P. Gayet, A. Fertin, J. Vollaire, Y. Usson, J.-L. Coll, V. Jossierand, *Int. J. Biol. Sci.* **2020**, *16*, 1616.
- [48] Y. Alapan, U. Bozuyuk, P. Erkoç, A. C. Karacakol, M. Sitti, *Sci. Rob.* **2020**, *5*, eaba5726.
- [49] P. E. Kinahan, D. W. Townsend, T. Beyer, D. Sashin, *Med. Phys.* **1998**, *25*, 2046.
- [50] A. Ale, V. Ermolayev, N. C. Deliolanis, V. Ntziachristos, *J. Biomed. Opt.* **2013**, *18*, 056006.
- [51] L. Kong, N. F. Rosli, H. L. Chia, J. Guan, M. Pumera, *Bull. Chem. Soc. Jpn.* **2019**, *92*, 1754.
- [52] X. Yan, Q. Zhou, M. Vincent, Y. Deng, J. Yu, J. Xu, T. Xu, T. Tang, L. Bian, Y.-X. J. Wang, K. Kostarelos, L. Zhang, *Sci. Rob.* **2017**, *2*, eaaq1155.
- [53] S. Tang, F. Zhang, H. Gong, F. Wei, J. Zhuang, E. Karshalev, B. de Ávila, C. Huang, Z. Zhou, Z. Li, L. Yin, H. Dong, R. H. Fang, X. Zhang, L. Zhang, J. Wang, *Sci. Rob.* **2020**, *5*, eaba6137.
- [54] M. Earle, G. De Portu, E. Devos, *Afr. J. Emerg. Med.* **2016**, *6*, 18.
- [55] R. A. O. Jaime, R. L. Q. Basto, B. Lamien, H. R. B. Orlande, S. Eibner, O. Fudym, *Procedia Eng.* **2013**, *59*, 30.
- [56] R. M. Souza, T. Q. Santos, D. P. Oliveira, R. M. Souza, A. V. Alvarenga, R. P. B. Costa-Felix, *J. Phys.: Conf. Ser.* **2016**, *733*, 012044.